Journal of Manufacturing Processes 25 (2017) 323–339

Contents lists available at ScienceDirect

Journal of Manufacturing Processes

journal homepage: www.elsevier.com/locate/manpro

Transient model of heat transfer and material flow at different stages of friction stir welding process

L. Shi, C.S. Wu*

MOE Key Lab for Liquid–Solid Structure Evolution and Materials Processing,and Institute of Materials Joining, Shandong University, Jinan 250061, China

ARTICLE INFO

Article history:
Received 16 June 2016
Received in revised form 19 October 2016
Accepted 8 November 2016
Available online 8 January 2017

Keywords:
Transient model
Friction stir welding
Heat generation
Material flow
Heat transfer

ABSTRACT

A better understanding of heat transfer and material flow for different stages (including plunge stage, dwell stage, welding stage, and cooling stage) of friction stir welding process is critical for the tool design and selecting appropriate welding variables. In this study, a transient model is developed to quantitatively analyze the dynamic variations of the heat generation, temperature profile and material flow for different stages of friction stir welding process, and is used to investigate the dependence of these aspects on the process parameters such as welding speed and the tool rotation speed. It is found that the total heat generation increases persistently during the plunge stage and reaches its peak value when the FSW tool shoulder contacts with the top surface of the workpiece. From the peak value, the total heat generation decreases monotonically during the dwell stage before attaining the quasi-steady state in the welding stage. The materials flow analysis predicts that the plastically deformed material in the front of the tool flows in counter-clockwise direction, passes the tool on the retreating side and gets released behind the tool during the welding stage. The model is experimentally validated by comparing the measured tool torque and peak temperature values with the predicted results, which agree well with each other.

© 2016 The Society of Manufacturing Engineers. Published by Elsevier Ltd. All rights reserved.

1. Introduction

Nowadays a large demand for lightweight, fuel-efficient and low emissive structures has been fulfilled by the widespread application of aluminum and magnesium alloys in manufacturing industries. As a solid-state joining process, friction stir welding (FSW) is considered as an energy efficient, environment friendly and versatile method of joining the lightweight materials than the fusion welding processes [1–4]. The FSW process involves four main stages: plunge stage, dwell stage, welding stage and cooling stage, as shown in Fig. 1. The process is initiated with the plunge stage during which a rotating tool, comprising a shoulder and a pin, is gradually penetrated into the abutting edges of workpieces until the shoulder contacts with their top surfaces. Next is the dwell stage during which the plunged tool is continued to rotate for a while to soften the material near the tool. This is followed by the welding stage during which the rotating tool is translated along the abutting edges, resulting in a weld joint. When the weld distance is covered, the tool is immediately pulled out of the workpiece which results in a rapid decrease in the temperature of the joint. This is referred to as the cooling stage.

During the FSW process, the heat energy is generated by friction between the tool and the workpiece, and plastic deformation of the workpiece [5–7]. While the heat energy softens the material in the shear layer around the tool, the plastic material flow in the shear layer produces localized viscous dissipation heat energy. Combination of the tool rotation and translation leads the softened material to flow from the front of the tool (leading side) to the back of the tool (trailing side), where it is forged into a joint. In FSW process, both the heat generation and material flow have crucial effects on the metallurgical characteristics and mechanical properties of the weld joints [8–10]. Furthermore, the preheating effects of the plunge and dwell stages have significant effect on the welding force and tool wear [11]. Therefore, a complete understanding of both the heat generation and material flow at different stages of FSW process is imperative in optimizing the process, and controlling microstructures and properties of the joints.

Numerical modeling of the FSW phenomena is powerful for understanding different phenomenon [4,12]. Several models have been developed to explore the heat generation and material flow phenomena in FSW process [12–28]. Some of them dealt only with the thermal conduction and ignored the material flow [13–15]. Others rightly emphasized the coupling of heat transfer and mate-

* Corresponding author. Fax: +86 531 8839 2711.
E-mail address: wucs@sdu.edu.cn (C.S. Wu).

http://dx.doi.org/10.1016/j.jmapro.2016.11.008
1526-6125/© 2016 The Society of Manufacturing Engineers. Published by Elsevier Ltd. All rights reserved.

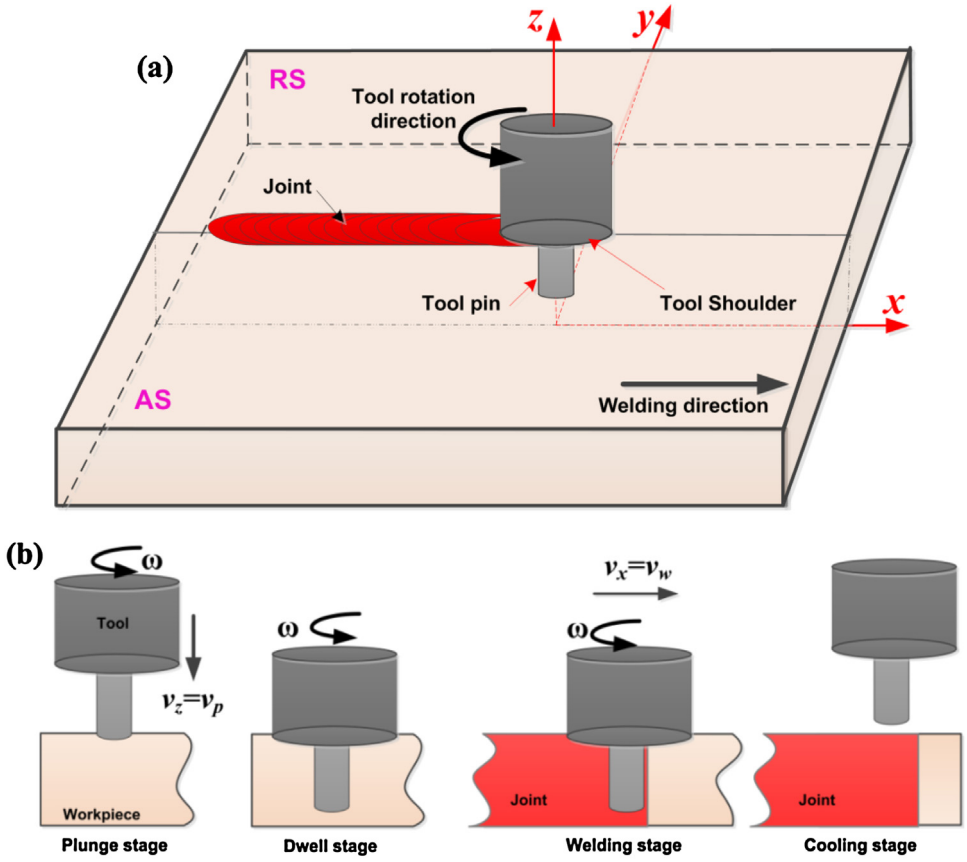


Fig 1. Schematic drawings of (a) friction stir welding (FSW) process, (b) different stages in FSW.

rial flow in the FSW process but limited the analysis only to the quasi-steady state of the welding stage and paid no attention to the plunge and dwell stages [16–21]. There are lots of situations where the steady-state conditions cannot be established, for example, at the start and the end of the welding process, or with varying process conditions/workpiece geometry [22]. Furthermore, the heat transfer and material flow during the plunge and dwell stages have significant effects on the properties of the joints and tool wear [11]. A thorough understanding of different stages of FSW process is important in the development of tools and processes for successfully welding of materials with high melting point [4]. Therefore, a transient numerical model is required for those common cases.

Several transient numerical models have recently been proposed to analyze the process mechanism at different stages of FSW [22–25]. Song and Kovacevic [23] and Zhang et al. [24,25] developed 3D transient thermal models which did not account for the convective heat transfer and heat generation from plastic deformation. Recently, Yu et al. [22] proposed a 3D transient model and investigated the heat transfer and material flow in friction stir processing of magnesium alloys. However, this model considered the heat generation only from the plastic deformation by assuming a full sticking condition at the tool-workpiece contact interfaces. In FSW process, the heat generation, the heat transfer and the plastic material flow pattern are fully coupled [26–28], and both friction heat and plastic deformation heat generate in the FSW process [27–30]. However, the transient numerical models mentioned above either only consider friction heat or only consider plastic deformation heat. None of these models adequately accounted for both heat transfer and material flow at different stages of FSW process. In addition, the tool torque is much higher at the start of the process when the tool comes into contact and is inserted into the workpiece at the plunge stage [31–33]. The detailed dynamic variation of tool torque at different stages of FSW is still unrevealed, and the available transient model which could be used to analyze the dynamic variation of tool torque at different stages of FSW is still limited. Therefore, a quantitative analysis of the tool torque, heat generation and material flow at different stages of FSW process is still needed.

In this study, a transient model is developed to quantitatively analyze the heat generation, heat transfer, and material flow during the four stages of the FSW process. Both the friction heat and the plastic deformation heat are considered to determine the heat flux distribution at the tool-workpiece contact interfaces. The effects of process parameters on the contact condition and the friction coefficient between tool-workpiece contact interfaces are examined. The model is validated by comparing the measured tool torque and peak temperature with the predicted results.

2. Formulation

2.1. Governing equations

Fig. 2 shows the geometric model for the simulation of FSW process. A moving coordinate system is established on the plate. During the plunge stage, the origin of the coordinate system is located at the intersection of the bottom surface of the workpiece and the axis of the tool. The welding direction is parallel to the positive *x*-axis, and the *z*-axis is along the plate thickness (upward). For simplification, the shoulder surface is assumed to be flat, and the thread on the pin side surface is not considered. The influence of the flash produced during the process is ignored. The FSW tool is treated as a rigid body and is not included in the model for saving computation time. The material flow is treated to be non-Newtonian, incompressible, laminar, and visco-plastic in nature [16–18]. The

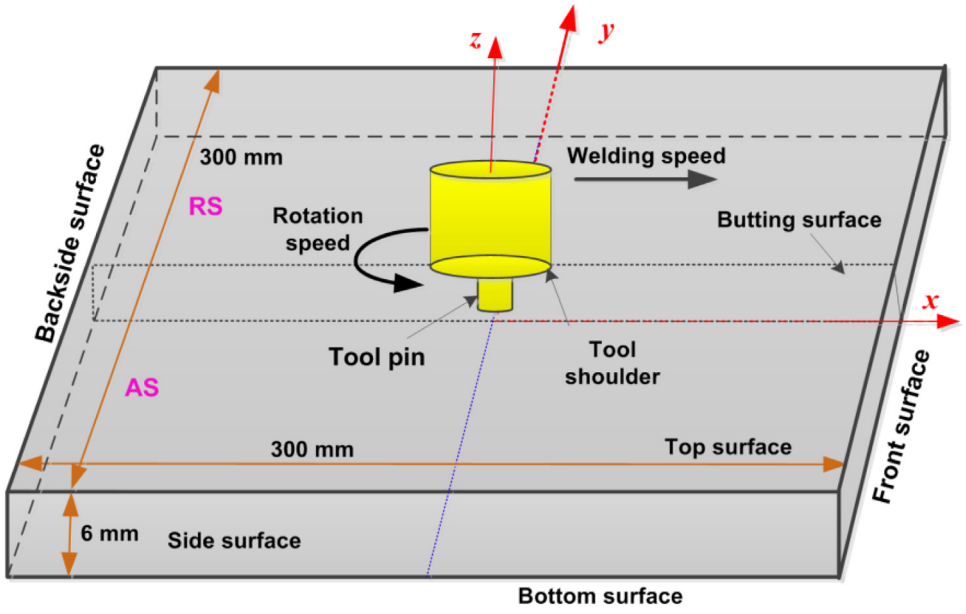


Fig. 2. Geometric model in the simulation.

governing equations for the 3D transient heat transfer and material flow are given as follows:

The continuity equation of the material flow

$$\frac{\partial \rho}{\partial t}+\frac{\partial u}{\partial x}+\frac{\partial v}{\partial y}+\frac{\partial w}{\partial z}=0 \tag{1}$$

where u, v, w are the material flow velocity in x, y, z direction, respectively.

The momentum equations

$$\frac{\partial(\rho u)}{\partial t}+\rho\left((u-v_w)\frac{\partial u}{\partial x}+v\frac{\partial u}{\partial y}+w\frac{\partial u}{\partial z}\right)=-\frac{\partial p}{\partial x}+\frac{\partial}{\partial x}\left(\mu\frac{\partial u}{\partial x}\right)+\frac{\partial}{\partial y}\left(\mu\frac{\partial u}{\partial y}\right)+\frac{\partial}{\partial z}\left(\mu\frac{\partial u}{\partial z}\right) \tag{2}$$

$$\frac{\partial(\rho v)}{\partial t}+\rho\left((u-v_w)\frac{\partial v}{\partial x}+v\frac{\partial v}{\partial y}+w\frac{\partial v}{\partial z}\right)=-\frac{\partial p}{\partial y}+\frac{\partial}{\partial x}\left(\mu\frac{\partial v}{\partial x}\right)+\frac{\partial}{\partial y}\left(\mu\frac{\partial v}{\partial y}\right)+\frac{\partial}{\partial z}\left(\mu\frac{\partial v}{\partial z}\right) \tag{3}$$

$$\frac{\partial(\rho w)}{\partial t}+\rho\left((u-v_w)\frac{\partial w}{\partial x}+v\frac{\partial w}{\partial y}+w\frac{\partial w}{\partial z}\right)=-\frac{\partial p}{\partial z}+\frac{\partial}{\partial x}\left(\mu\frac{\partial w}{\partial x}\right)+\frac{\partial}{\partial y}\left(\mu\frac{\partial w}{\partial y}\right)+\frac{\partial}{\partial z}\left(\mu\frac{\partial w}{\partial z}\right) \tag{4}$$

where ρ is the density, p is the pressure, v_w is the welding speed, and μ is the non-Newtonian viscosity which will be detailedly described in the following section.

The energy equation

$$\frac{\partial(\rho C_p T)}{\partial t}+\rho C_p\left((u-v_w)\frac{\partial T}{\partial x}+v\frac{\partial T}{\partial y}+w\frac{\partial T}{\partial z}\right)=\frac{\partial}{\partial x}\left(k\frac{\partial T}{\partial x}\right)+\frac{\partial}{\partial y}\left(k\frac{\partial T}{\partial y}\right)+\frac{\partial}{\partial y}\left(k\frac{\partial T}{\partial y}\right)+S_v \tag{5}$$

where T is the temperature, k is the thermal conductivity, C_p is the specific heat of the material. S_v is the viscous dissipation heat generation due to plastic material flow originated by high strain rate inside the shear zone of the workpiece near the tool. The volumetric heat energy density can be expressed as [16–18]:

$$S_v=f_m\mu\Phi \tag{6}$$

where f_m is an arbitrary constant which represents the extent of atomic mixing in the shear zone and Φ is given as follows [16–18]:

$$\Phi=2\left(\left(\frac{\partial u}{\partial x}\right)^2+\left(\frac{\partial v}{\partial y}\right)^2+\left(\frac{\partial w}{\partial z}\right)^2\right)+\left(\frac{\partial u}{\partial y}+\frac{\partial v}{\partial x}\right)^2+\left(\frac{\partial u}{\partial z}+\frac{\partial w}{\partial x}\right)^2+\left(\frac{\partial w}{\partial y}+\frac{\partial v}{\partial z}\right)^2 \tag{7}$$

2.2. Constitutive model and viscosity

Viscosity has significant influence on the heat generation and material flow behaviors which in turn affect the value of viscosity [34–36]. In this model, the Zener–Holloman constitutive law proposed by Sellars and Tegart [37] is used to describe the relationship between the strain rate, flow stress and temperature as follows:

$$Z=\dot{\bar{\varepsilon}}\exp\left(\frac{Q}{RT}\right)=A(\sinh\ \alpha\sigma)^n \tag{8}$$

where Z is Zener–Holloman parameter, $\dot{\bar{\varepsilon}}$ is the effective strain rate during FSW [36], Q is the activation energy of the workpiece material, R is the gas constant, A and α are material constant, n is stress exponent. All the materials constants in the constitutive equation are determined from plastic deformation [38]. From Eq. (8), the flow stress of the material in FSW process can be calculated as:

$$\sigma=\frac{1}{\alpha}\sinh^{-1}\left[\left(\frac{\dot{\bar{\varepsilon}}}{A}\exp\left(\frac{Q}{RT}\right)\right)^{1/n}\right] \tag{9}$$

Finally, the expression of viscosity used in this model is written as:

$$\mu=\frac{1}{3\alpha\dot{\bar{\varepsilon}}}\sinh^{-1}\left[\left(\frac{\dot{\bar{\varepsilon}}}{A}\exp\left(\frac{Q}{RT}\right)\right)^{1/n}\right] \tag{10}$$

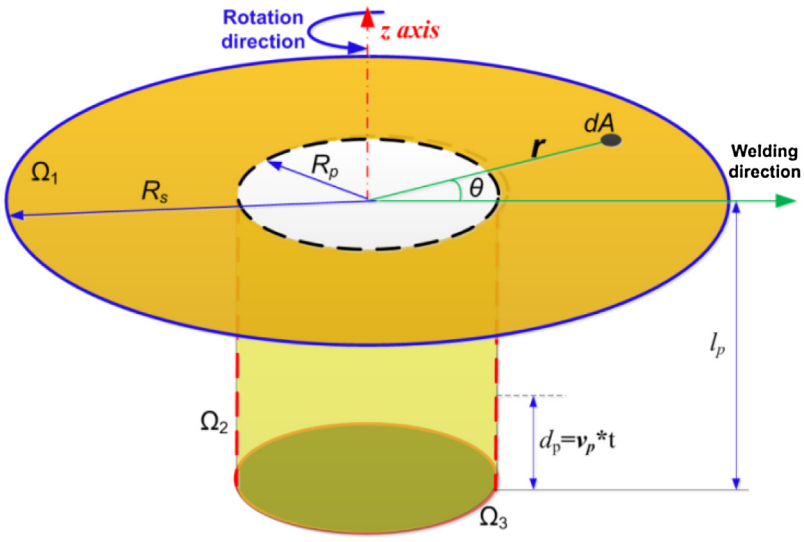


Fig. 3. A schematic illustration of tool-workpiece contact interfaces in FSW process.

2.3. Interfacial heat source model

During FSW process, sliding between the tool-workpiece contact interfaces lead to the generation of friction heat, while the heat due to plastic deformation is produced by the shear stress near the tool [16–18]. In addition, the viscous dissipation heat generation due to plastic material flow originated by high strain rate near the tool accounts for ~4% of the total heat generation [16,17]. A schematic of the tool-workpiece contact interfaces in FSW process is shown in Fig. 3. As shown in the figure, the possible sources of heat energy are the shoulder-workpiece contact interface (Ω_1 region), the pin side-workpiece contact interface (Ω_2 region), and the pin bottom-workpiece contact interface (Ω_3 region).

The heat flux distribution at the tool-workpiece contact interfaces is calculated as [34]:

$$q(r) = \left[\eta(1-\delta)\tau_c + \beta\delta\mu_f P_N\right](\omega r - v_w \sin\theta) \tag{11}$$

where η is the conversion efficiency of deformational work into heat energy, τ_c is the contact shear stress, β is the friction heat conversion efficiency, i.e., the percentage of mechanical friction converted to heat energy. μ_f is the friction coefficient at the tool-workpiece contact interfaces, P_N is the plunge pressure of the tool, ω is the rotation speed of the tool, r is the radial distanse from the tool axis, θ is the angle between the welding direction and the r radius vector direction as shown in Fig. 3, while δ is the contact state variable at tool-workpiece contact interfaces which is defined as:

$$\delta = 1 - \frac{\omega_m}{\omega_t} \tag{12}$$

where ω_t is the rotating speed of the tool at the contact area and ω_m represents the rotation speed of the plastic material. The value of δ ranges from 0 to 1, depending on the tool-workpiece contact condition. For a value of $\delta = 0$, there is no sliding at the tool-workpiece contact interfaces. In this state, all the plastic material at the interface sticks to the tool and rotates with its rotation speed. For a fully sliding state without plastic deformation, $\delta = 1$, there is no plastic material sticking to the tool. The condition $0 < \delta < 1$ represents partial sticking or sliding at the tool-workpiece contact interfaces. In this study, a partial sticking condition is assumed at the tool-workpiece contact interfaces during the FSW process. Furthermore, the influence of the process parameters on the contact state variable and friction coefficient at tool-workpiece contact interfaces is taken into consideration in the model. The contact state variable and friction coefficient are given by the following equations [39]:

$$\delta = 0.31 \times \exp\left(\frac{\omega r}{1.87}\right) - 0.026 \tag{13}$$

$$\mu_f = 0.5 \times \exp(-\delta\omega r) \tag{14}$$

The contact shear stress can be estimated by the following equation based on the von Mises yield criterion.

$$\tau_c = \frac{\sigma_y}{\sqrt{3}} \tag{15}$$

where σ_y is the yield stress of the workpiece.

Eq. (11) is used for calculating the interfacial heat energy density at the shoulder-workpiece contact interface (i.e., Ω_1 region) and the pin bottom-workpiece contact interface (i.e., Ω_3 region). Since the cylindrical tool pin is used, the normal pressure at the pin side surface which is approximately equal to the yield stress of the plastic material [40,41], which is different from that at the shoulder and pin bottom surface. The heat flux distribution at the pin side-workpiece contact interface (i.e., Ω_2 region) can be estimated as:

$$q_{ps} = \left[\eta(1-\delta)\tau_c + \beta\delta\mu_f\sigma_y\right](\omega R_p - v_w \sin\theta) \tag{16}$$

where R_p is the radius of the tool pin.

The total heat generation at the shoulder can be described by:

$$Q_s = \begin{cases} \int_0^{2\pi}\int_{R_p}^{R_s} q(r)rdrd\theta & \text{for } t_p \le t \le t_w \\ 0 & \text{Otherwise} \end{cases} \tag{17}$$

where R_s is the radius of the tool shoulder, t_p is the finish time for the plunge stage and t_w is the finish time for the welding stage.

Similarly, the total heat generation at the pin bottom surface can be given as:

$$Q_{pb} = \begin{cases} \int_0^{2\pi}\int_0^{R_p} q(r)rdrd\theta & \text{for } 0 < t \le t_w \\ 0 & \text{Otherwise} \end{cases} \tag{18}$$

The total heat generation at pin side surface can be estimated as:

$$Q_{ps} = \begin{cases} \int_0^{2\pi} \int_{d-d_p}^{d} q_{ps} R_p dz d\theta & \text{for } 0 < t \le t_w \\ 0 & \text{Otherwise} \end{cases} \quad (19)$$

where d is the thickness of the workpiece, and d_p is the plunge depth of the tool pin, which is given as:

$$d_p = \begin{cases} v_p t & \text{for } 0 < t < t_p \\ l_p & \text{for } t_p \le t \le t_w \\ 0 & \text{Otherwise} \end{cases} \quad (20)$$

where v_p is the plunge speed and l_p is the pin length as shown in Fig. 3.

2.4. Tool torque model

The torque experienced by the tool due to its rotational motion is fully coupled with the tool-workpiece contact condition and heat energy generation in the FSW process [16–18]. The total torque can be calculated by the sliding and sticking components of the torque [19]. The total torque at an element area dA can be calculated as [19]:

$$M = \int_A r \times \left[(1-\delta)\tau_c + \delta\mu_f P_N\right] dA \quad (21)$$

Then, the torque at the shoulder can be expressed as:

$$M_s = \begin{cases} \int_0^{2\pi} \int_{R_p}^{R_s} \left[(1-\delta)\tau_c + \delta\mu_f P_N\right] r^2 dr d\theta & \text{for } t_p \le t \le t_w \\ 0 & \text{Otherwise} \end{cases} \quad (22)$$

Similarly, the torque at the tool pin side and pin bottom surfaces can be calculated from Eqs. (23) and (24), respectively.

$$M_{ps} = \begin{cases} \int_0^{2\pi} \int_{d-d_p}^{d} \left[(1-\delta)\tau_c + \delta\mu_f \sigma_y\right] R_p^2 dz d\theta & \text{for } 0 < t \le t_w \\ 0 & \text{Otherwise} \end{cases} \quad (23)$$

$$M_{pb} = \begin{cases} \int_0^{2\pi} \int_{0}^{R_p} \left[(1-\delta)\tau_c + \delta\mu_f P_N\right] r^2 dr d\theta & \text{for } 0 < t \le t_w \\ 0 & \text{Otherwise} \end{cases} \quad (24)$$

Finally, the total torque in FSW process is expressed as:

$$M_{total} = M_s + M_{ps} + M_{pb} \quad (25)$$

2.5. Boundary conditions

The transient model is developed to analyze all the four stages during the FSW process. Since the tool is rapidly pulled out of the workpiece after the welding stage, it has little influence on the heat transfer and material flow during the cooling stage. The initial temperature of the material and the ambient temperature are assumed to be 300 K. The heat and velocity boundary conditions for the tool-workpiece contact interfaces are described in details as follows.

2.5.1. Plunge stage

During the plunge stage, the rotating tool pin penetrates into the workpiece until the shoulder contacts with the top surface of workpiece. The heat boundary condition at the shoulder-workpiece contact interface is given as:

$$k\frac{\partial T}{\partial z} = \begin{cases} \sigma_r \varepsilon_r (T^4 - T_a^4) - \gamma_t (T - T_a) & (0 < t < t_p) \\ \frac{J_W}{J_W + J_T} q(r) & (t = t_p) \end{cases} \quad (26)$$

where σ_r is the Stefan-Boltzmann constant, ε_r is the external emissivity, γ_t is the heat transfer coefficient at the top of the workpiece, and T_a is the ambient temperature. J_W and J_T are the thermal effusivity of the workpiece and tool respectively. J is given as:

$$J = \sqrt{k\rho C_p} \quad (27)$$

The heat boundary condition at the pin side-workpiece contact interface is given as:

$$k\frac{\partial T}{\partial n} = \frac{J_W}{J_W + J_T} q_{ps} \quad (0 < t \le t_p, d - d_p \le z \le d) \quad (28)$$

Similarly, the heat boundary condition at the pin bottom-workpiece contact interface is given as:

$$k\frac{\partial T}{\partial z} = \frac{J_W}{J_W + J_T} q(r) \quad (0 < t \le t_p) \quad (29)$$

At the top surface beyond the shoulder-workpiece contact interface, both convective and radiative heat transfer are considered and the heat boundary condition is expressed in the following form:

$$-k\frac{\partial T}{\partial z} = \sigma_r \varepsilon_r (T^4 - T_a^4) + \gamma_t (T - T_a) \quad (30)$$

On the side surface and the bottom surface of the workpiece, there is intimate contacts of the workpiece with the clamping equipment and the backing plate. Therefore, only the convective heat transfer is considered. The heat boundary condition is represented in the following form:

$$k\frac{\partial T}{\partial n} = \gamma_b (T - T_a) \quad (31)$$

All the side surface, bottom surface and top surface of workpiece beyond the tool-workpiece contact interfaces are considered as stationary boundaries, i.e., $v_x = v_y = v_z = 0$. At the shoulder-workpiece contact interface, the velocity boundary condition is $v_x = v_y = v_z = 0$ for $0 < t < t_p$. When $t = t_p$, the shoulder contacts with the top surface of the workpiece and the velocity boundary condition at the shoulder-workpiece contact interface is given as [16,17]:

$$\begin{cases} v_x = (\delta - 1)\omega r \sin\theta \\ v_y = (\delta - 1)\omega r \cos\theta \\ v_z = 0 \end{cases} \quad (32)$$

Eq. (32) is also used as the velocity boundary condition at the pin bottom-workpiece contact interface. At the pin side-workpiece contact interface, the velocity boundary condition is given as:

$$\begin{cases} v_x = (\delta - 1)\omega r \sin\theta \\ v_y = (\delta - 1)\omega r \cos\theta \quad (0 < t < t_p) \\ v_z = (1 - \delta) v_p \end{cases} \quad (33)$$

At $t = t_p$, the velocity boundary condition at pin side-workpiece contact interface is similar to the tool shoulder as shown in Eq. (32).

2.5.2. Dwell and welding stages

During the dwell stage, the tool pin fully penetrates into the workpiece, and the tool shoulder contacts with the workpiece. The heat flux boundary conditions and velocity boundary conditions are

similar to those in the plunge stage at $t = t_p$ as described in Section 2.5.1.

After the dwell stage, the tool traverses along the abutting edges with a welding speed. In order to consider the translation of the tool and to reduce the computation time, the moving coordinate system is used instead of the dynamic mesh method [22]. The coordinate system moves on the workpiece along the negative x-axis with the welding speed. During the welding stage, the heat flux boundary conditions at tool-workpiece contact interfaces are similar to those in the plunge stage at $t = t_p$ as described in Section 2.5.1. Other heat boundary conditions are the same as those in the plunge stage as described in Section 2.5.1. During the welding stage, the material flows into the calculation domain from the front surface at the welding speed, while it flows out of the calculation domain through the back surface. On the other boundaries (side, top and bottom surfaces of the workpiece) beyond the tool-workpiece contact interfaces, a moving wall boundary condition with the welding speed is applied.

2.5.3. Cooling stage

During the cooling stage, the boundary conditions are modified as follows. The material flow velocity is reset to zero at all the tool-workpiece contact interfaces and the surfaces of the workpiece. The heat flux boundary conditions at the tool-workpiece contact interfaces are removed and replaced with a convective and radiative heat transfer boundary condition in the following form,

$$k\frac{\partial T}{\partial n} = \sigma_r \varepsilon_r (T^4 - T_a^4) + \gamma_t (\mathrm{T} - T_a) \tag{34}$$

2.6. Numerical solution method

To conduct the numerical simulation of different stages of FSW process, all the governing equations and the boundary conditions are solved by employing finite volume method by using the commercial CFD code FLUENT. The calculated domain is 300 mm in length, 300 mm in width and 6 mm in thickness. Non-uniform grid system is used to discretize the calculation domain. Finer grids are chosen to describe the portion of the domain with severe material flow and heat energy evolution near the tool. For example, the mesh size near the pin is Δx =0.2 mm, Δy =0.2 mm, Δz =0.2 mm to capture the material flow velocity correctly. The grid dependence study is conducted, and the calculation accuracy is found independent on the grid system. The design and number of mesh elements are determined by considering both the efficiency and the accuracy of the computation. The mesh system for finite volume calculation is shown in Fig. 4. The SIMPLEC algorithm is used for solving the governing equations [42]. Second order upwind scheme is used for the discretization of the momentum equations and energy equation. A dynamic mesh is used to capture the heat and material flow during the plunge of the tool pin. In hexahedral mesh zone, the dynamic layering method could be used to add or remove layers of cells adjacent to a moving boundary according to the height of the layer adjacent to the moving surface [43]. In this transient model of FSW, the dynamic layering mesh method is used to update the volume mesh in the deforming workpiece subject to the motion defined at the tool pin side and pin bottom surfaces. The cells in the layer adjacent to the FSW tool bottom would compress and finally vanish as the tool pin penetrates into the workpiece. The plastic material overflowing to the top of the workpiece at the vanishing cell has been ignored in the model.

3. Experimental description

2024 aluminum alloy plates (300 mm in length, 300 mm in width, and 6 mm in thickness) were used to perform experimental and numerical investigations. The average tool torque at quasi-steady state welding stage was monitored and determined as reported in Ref. [44]. Meanwhile, K-type thermocouples were used to measure the peak temperature during the FSW process. In order to measure the temperature at certain locations, suitable holes were drilled from the top surface of the workpiece, and the thermocouples were put into the little holes and joined at the hole bottom. Detailed description of the temperature measurement in FSW process is given in Ref. [18]. The nominal chemical composition of the 2024 aluminum alloy is listed in Table 1. Table 2 lists the specific heat capacity and the thermal conductivity taken from Ref. [5]. The yield strength of 2024 aluminum alloy is written as [45]:

$$\sigma_y = \begin{cases} 30.324 + \dfrac{322.673}{1 + 10^{(-0.101441)\times(462.732 - T)}} & T < 644 \\ 69.424 - 0.216 \times T & T \geq 644 \end{cases} \text{(MPa)} \tag{35}$$

In this study, the shoulder diameter is 15.0 mm. The diameter of the cylindrical pin is 5.0 mm. The length of the pin is 5.7 mm. The other data used for the calculations are presented in Table 3. The FSW process parameters are summarized in Table 4. The experimentally measured tool torques and peak temperatures are compared with the calculated ones to verify the validity and reliability of the numerical model.

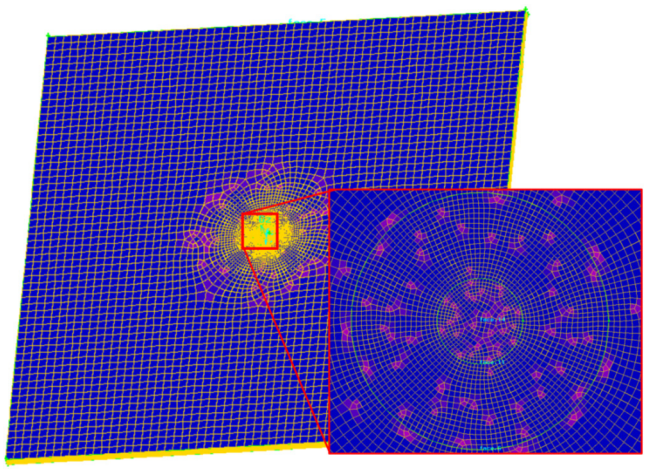


Fig. 4. The mesh system used for calculation (red frame area magnified the mesh near the tool). (For interpretation of the references to colour in this figure legend, the reader is referred to the web version of this article.)

Table 1
Chemical composition of 2024 aluminum alloy (wt%).

Element	Si	Fe	Cu	Mn	Mg	Ni	Zn	Ti	Al
wt.%	0.15	0.25	4.58	0.63	1.59	<0.10	0.20	<0.10	Balance

Table 2
Specific heat capacity and thermal conductivity of 2024 aluminum alloy.

Temperature (K)	290	373	473	573	673
Specific heat capacity/(J kg^{-1} K^{-1})	864.0	921	1047	1130	1172
Thermal conductivity/(W m^{-1} K^{-1})	120.0	134.4	151.2	172.2	176.4

4. Results and discussion

4.1. Transient heat generation

The new transient model is used to perform numerical simulation for different stages of FSW process. Fig. 5 shows the total heat generation during the FSW process and its constitution as a func-

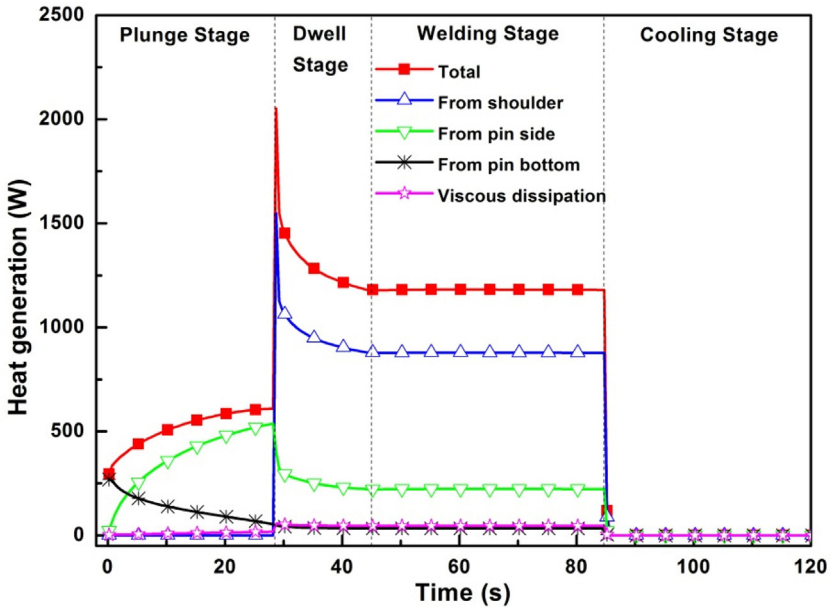


Fig. 5. Variation of the calculated heat generation during the FSW process (Case 1).

Table 3
Other data used in calculation.

Property/parameter	Value
Tool shoulder diameter (mm)	15.0
Pin diameter (mm)	5.0
Pin length (mm)	5.7
Workpiece density (kg/m^3)	2780
Workpiece incipient melting temperature (K)	775
Workpiece length (mm)	300
Workpiece width (mm)	300
Workpiece thickness (mm)	6.0
Tool density (kg/m^3)	7930
Specific heat of tool (J kg^{-1} K^{-1})	502
Thermal conductivity of tool (W m^{-1} K^{-1})	21.4
Plunge pressure (MPa)	30.0
Plunge speed (mm/min)	12
Finish time for the plunge stage (s)	28.5
Finish time for the dwell stage (s)	45.0
Finish time for the welding stage (s)	85.0
Friction heat conversion efficiency	0.95
Deformational work conversion efficiency	0.9
Arbitrary constant of viscous dissipation heat generation	0.05
Stefan-Boltzmann constant (W m^{-2} K^{-4})	5.670367×10^{-8}
Heat transfer coefficient at the bottom of the workpiece(W m^{-2} K^{-1})	300
Heat transfer coefficient at the side of the workpiece(W m^{-2} K^{-1})	200
Heat transfer coefficient at the top of the workpiece(W m^{-2} K^{-1})	50
External emissivity	0.2

Table 4
FSW process parameters.

Test Case	Rotation speed (rpm)	Welding speed (mm/min)
1	800	120
2	800	80
3	800	40
4	1000	120
5	1000	80
6	1000	40

tion of time, i.e., the heat generation from the shoulder, pin side, pin bottom and viscous dissipation. In this figure, the variation in heat generation during the different stages of the FSW process exhibits different trends. During the plunge stage, from $t = 0$ to $t_p = 28.5$ s, the total heat generation increases slowly with time. This is due to the increase in heat generation from the pin side with the increasing area of pin side-workpiece contact interface. However, the heat generation from the pin bottom decreases with time because the interfacial temperature at the contact interface increases resulting in lower heat from plastic deformation. The heat generation due to viscous dissipation marginally increases with time because of shear zone expansion. At the end of plunge stage, sharp increase in the total heat generation is observed with its peak value at $t_p = 28.5$ s (i.e.,when the shoulder contacts with the workpiece). During the dwell stage, from $t_p = 28.5$ s to $t_d = 45$ s (t_d is the end time of dwell stage), the increase in interfacial temperature at the tool-workpiece contact interfaces with time causes a decrease in the contact shear stress and the heat generation from plastic deformation. This ultimately results in a decrease in the total heat generation. During the welding stage, from $t_d = 45$ s to $t_w = 85$ s, the total heat generation is almost constant, and therefore the quasi-steady state is achieved. At the end of the welding stage or in the cooling stage, no heat is generated because the tool is pulled out of the workpiece.

Fig. 6 illustrates the transient heat generation at the tool-workpiece contact interfaces in the FSW process for Case 1. At $t = 4.5$ s, i.e., when the tool is plunged 0.9 mm into the workpiece, the interfacial heat density at the pin side surface is higher than 1.2×10^7 W/m^2 (Fig. 6a). As the pin continues to penetrate into the workpiece ($t = 15$ s), the interfacial heat density decreases slightly because the increasing interfacial temperature results in lower heat generation from plastic deformation (Fig. 6b). Fig. 6c shows the interfacial heat density just 0.3 s before the contact between shoulder and workpiece, and demonstrates similar trends as Fig. 6b. However, the peak interfacial heat density, at this instance, decreases to about 3.1×10^6 W/m^2 ($t = 28.2$ s). As observed before, the contact between the shoulder and workpiece causes the maximum total heat generation (Fig. 5). When the dwell stage is just initiated, i.e., at $t = 28.51$, the interfacial heat energy density reaches the maximum (1.51×10^7 W/m^2) and is located at the edge of the shoulder (Fig. 6d). It demonstrates that most of the total heat is generated at locations around the edge of the shoulder away from tool axis owing to the higher relative velocity

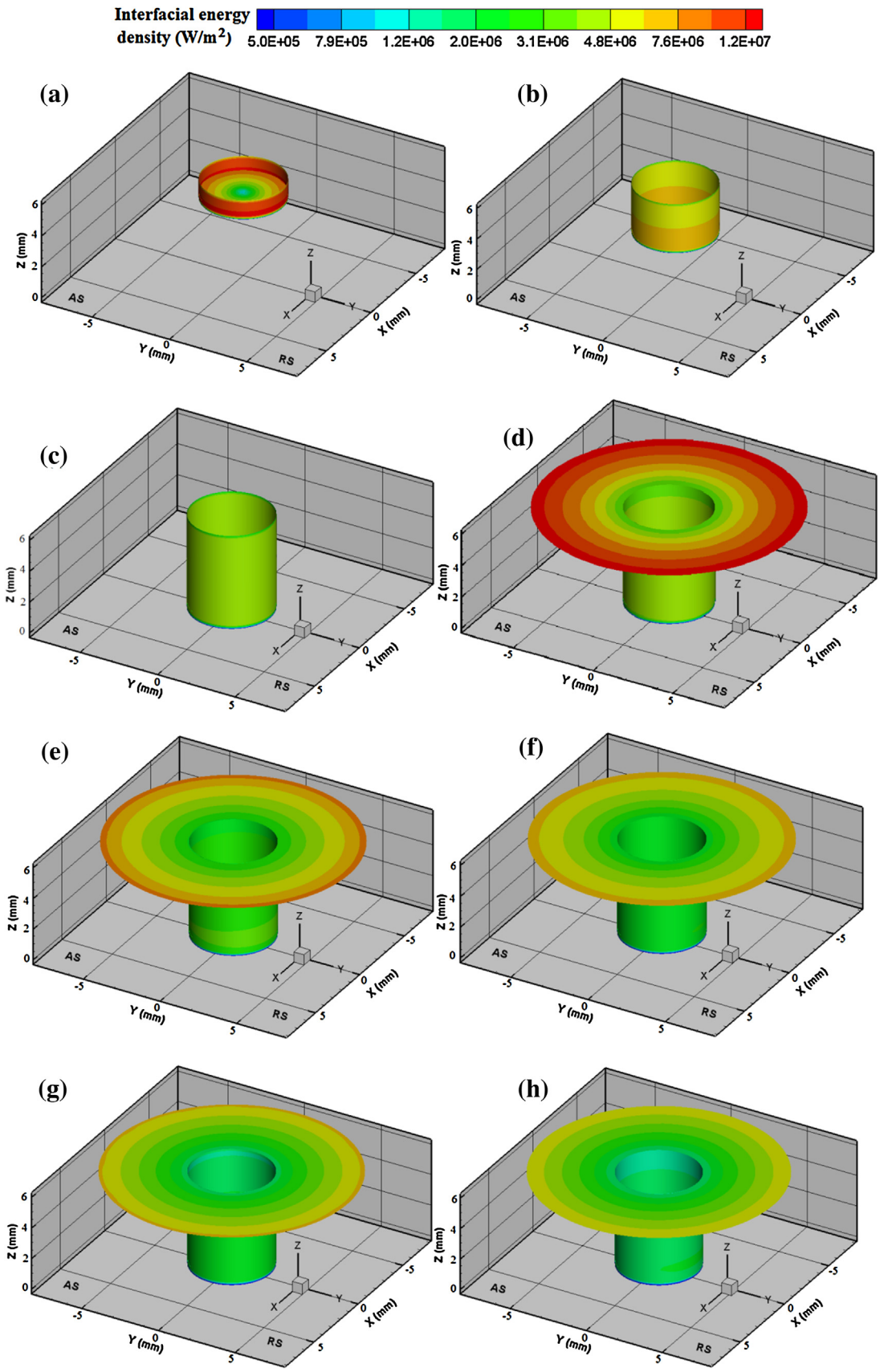


Fig. 6. The transient heat generation at tool-workpiece contact interfaces in FSW process (Case 1). (a) 4.5 s, (b) 15.0 s, (c) 28.2 s, (d) 28.51 s, (e) 28.8 s, (f) 30.0 s, (g) 36.9 s, (h) 45.0 s.

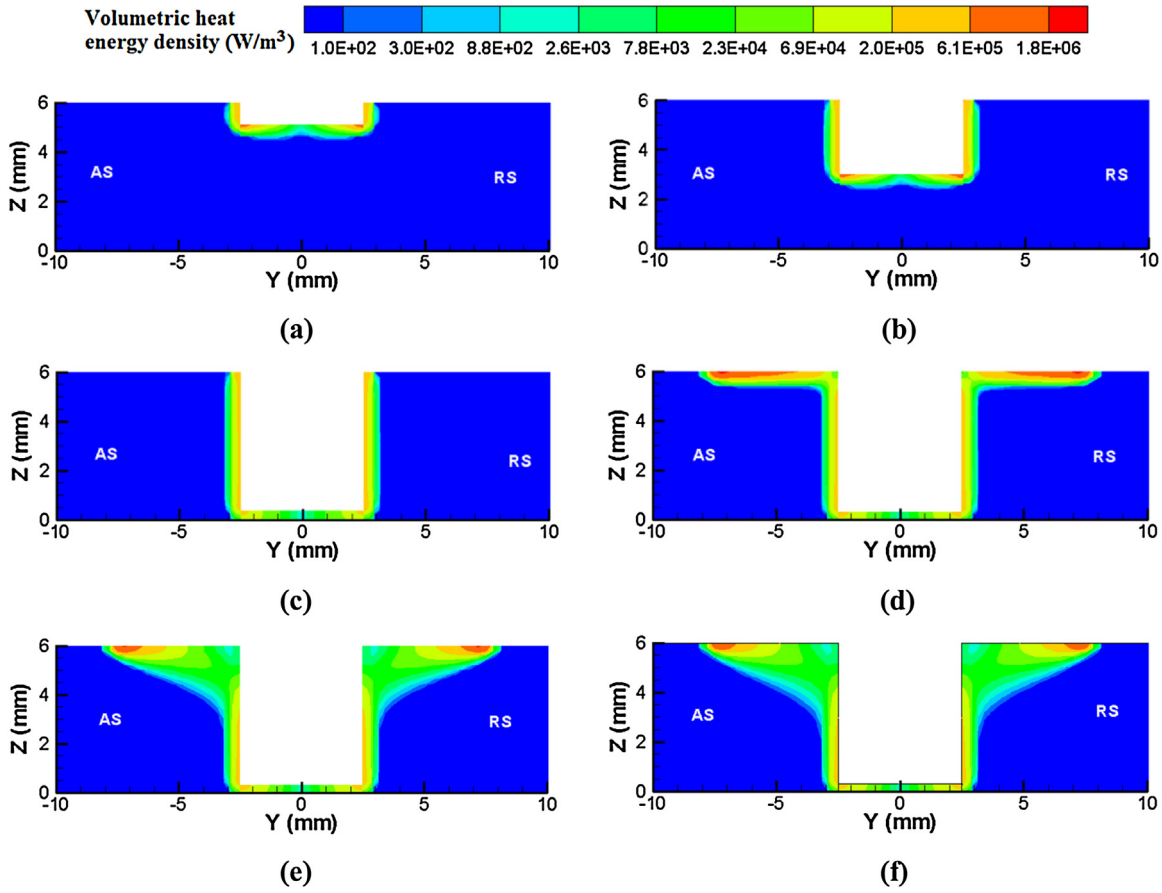


Fig. 7. The transient viscous dissipation heat generation in FSW process (transverse cross-section, Case 1). (a) 4.5 s, (b) 15.0 s, (c) 28.2 s, (d) 28.51 s, (e) 28.8 s, (f) 30.0 s.

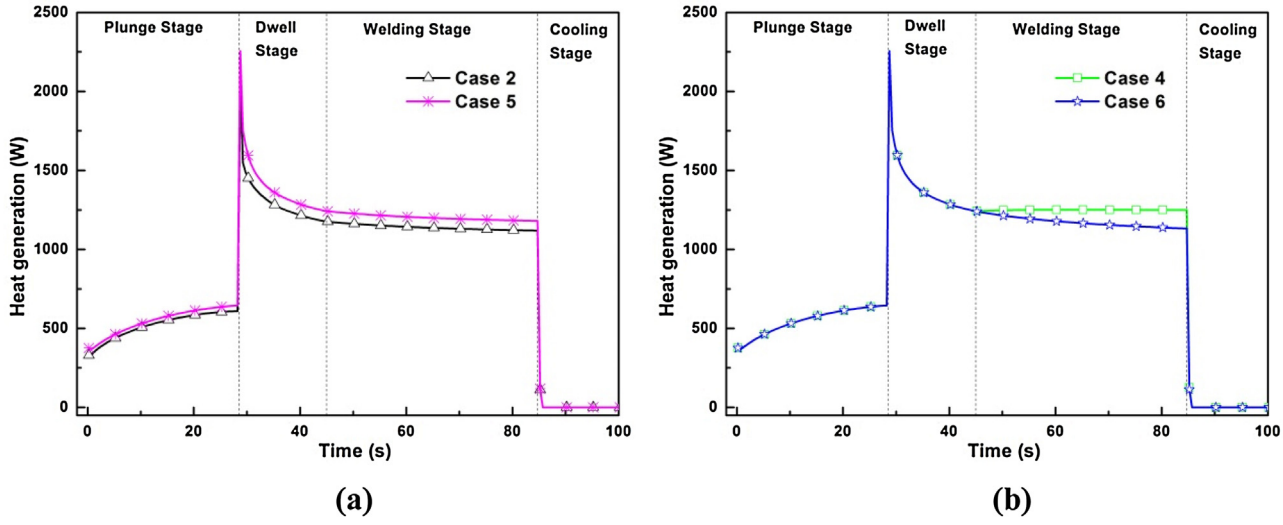


Fig. 8. The calculated total heat energy generation as a function of time during the FSW process at (a) different rotation speed and (b) different welding speed.

at the shoulder-workpiece contact interface. At $t = 28.8$ s, i.e., 0.3 s after the shoulder contacts with the workpiece, the peak value of interfacial heat density decreases to 7.6×10^6 W/m^2 (Fig. 6e). The interfacial heat density continues to decrease further during the dwell stage as shown in Fig. 6f and g. When $t = 45$ s, i.e., during the welding stage, the interfacial heat density remains almost constant (around 4.8×10^6 W/m^2), and a quasi-steady state is reached as shown in Fig. 6h.

Fig. 7 depicts the transient viscous dissipation heat in the FSW process. During the plunge stage, the viscous dissipation heat is generated only in a small shear zone near the tool pin, as shown in Fig. 7a–c. As the pin penetrates into the workpiece, expansion of shear zone causes slight increase in the viscous dissipation heat. After the shoulder-workpiece contact, the volumetric heat energy density under the shoulder increases rapidly with its maximum value located at the edge of the shoulder, as shown in Fig. 7d. This is because the strain rate and the viscosity in the shear zone are

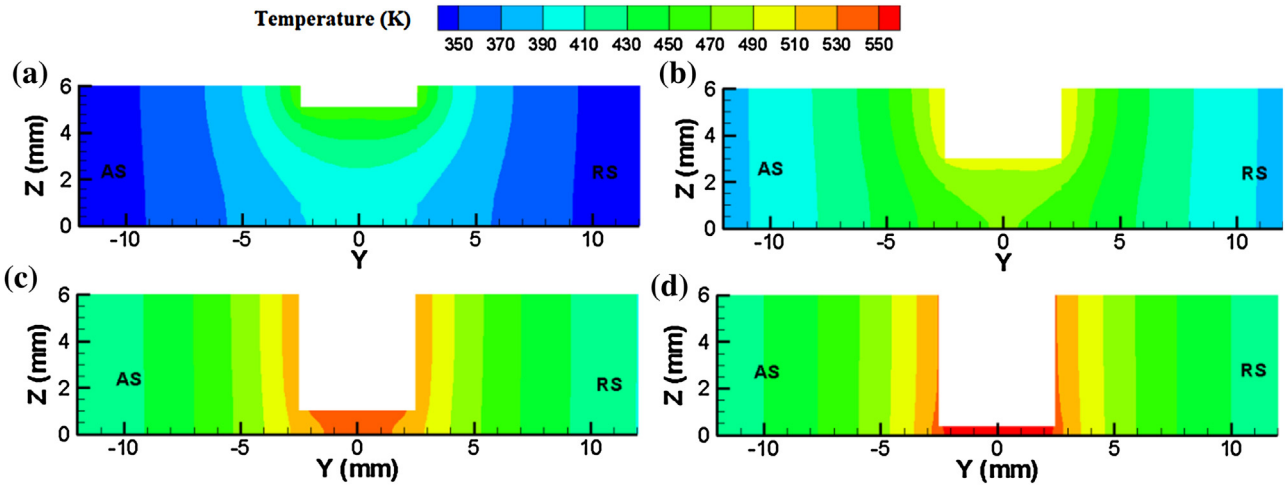


Fig. 9. The calculated temperature distribution at the transverse cross-section during the plunge stage (Case 1). (a) 4.5 s, (b) 15.0 s, (c) 24.9, (d) 28.2 s.

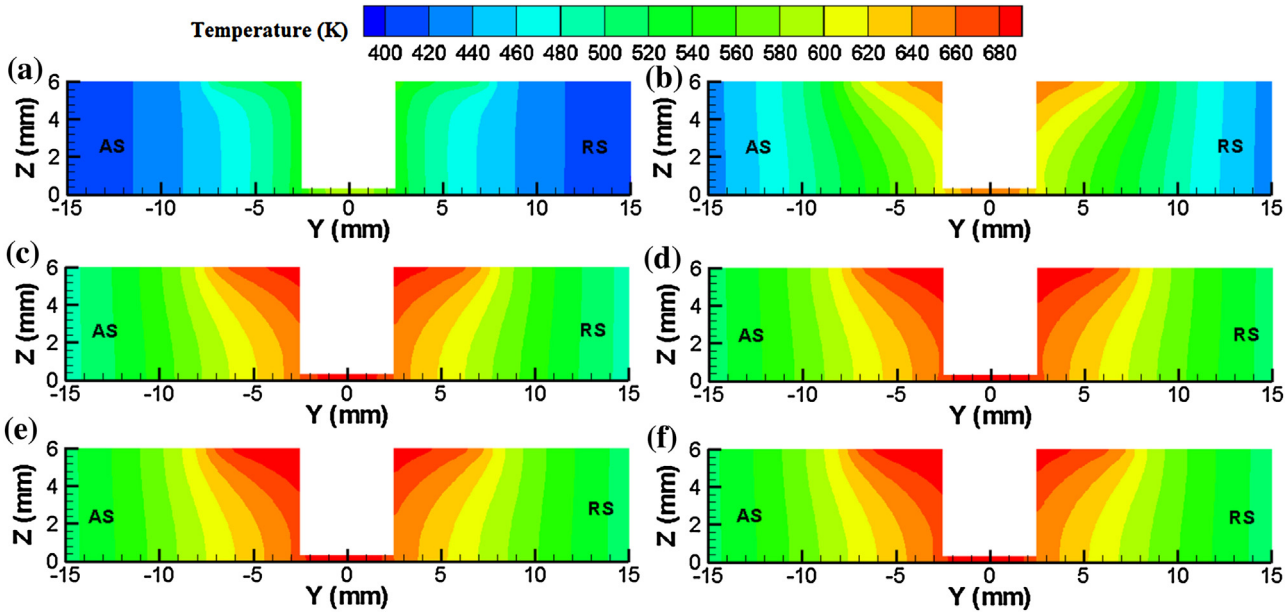


Fig. 10. The predicted temperature distribution at the transverse cross-section during the dwell and welding stages (Case 1). (a) 28.51 s, (b) 30.0 s, (c) 37.9 s, (d) 45.0 s, (e) 50.1 s, (f) 60.0 s.

the maximum at the shoulder edge. Shortly after the shoulder-workpiece contact, shear zone under the shoulder expands sharply and reaches the quasi-steady state, as shown in Fig. 7e and f. Generally, the viscous dissipation heat generation is relatively low. For Case 1, it is about 3.9% of the total heat generation which is consistent with the results in literature [16,17,46].

Fig. 8 shows the variation in calculated total heat generation as a function of time for specific process parameters. Fig. 8a shows that the total heat generation increases with the increasing tool rotation speed. The increase in tool rotation speed (from 800 rpm to 1000 rpm) causes an increase in the sliding velocity and shear strain rate, which in turn causes a rise in the interfacial heat density at the tool-workpiece contact interfaces and results in an increase in the total heat generation. Fig. 8b shows that the heat generations during the plunge stage and dwell stage are identical for Cases 4 and 6 because the same rotation speed was used in both the cases. However, the total heat generation is marginally higher in the welding stage for Case 4 (i.e., with a higher welding speed, 120 mm/min). At higher welding speed, the interfacial temperature decreases because heat is diffused over a relatively large region. However, at lower welding speeds, the raise in interfacial temperature causes localized softening that reduces the shear stress at the contact interfaces. This suppresses the plastic deformation heat generation and reduces total heat generation, as shown in Fig. 8b. Furthermore, the heat generation during the welding stage remains nearly constant for Case 4 whereas it decreases with time for Case 6. This indicates that it is easier to achieve steady state heat transfer at higher welding speeds (Case 4) when the other conditions are unchanged.

4.2. Transient temperature distribution

Fig. 9 shows the calculated temperature distribution at the transverse cross-section near the tool during the plunge stage. As the pin penetrates into the workpiece, the temperature near the tool goes up. At the initial plunge stage (Fig. 9a and b), the hottest region is located at the pin-workpiece contact interfaces and the isothermals near the tool are tapered from the top surface to the

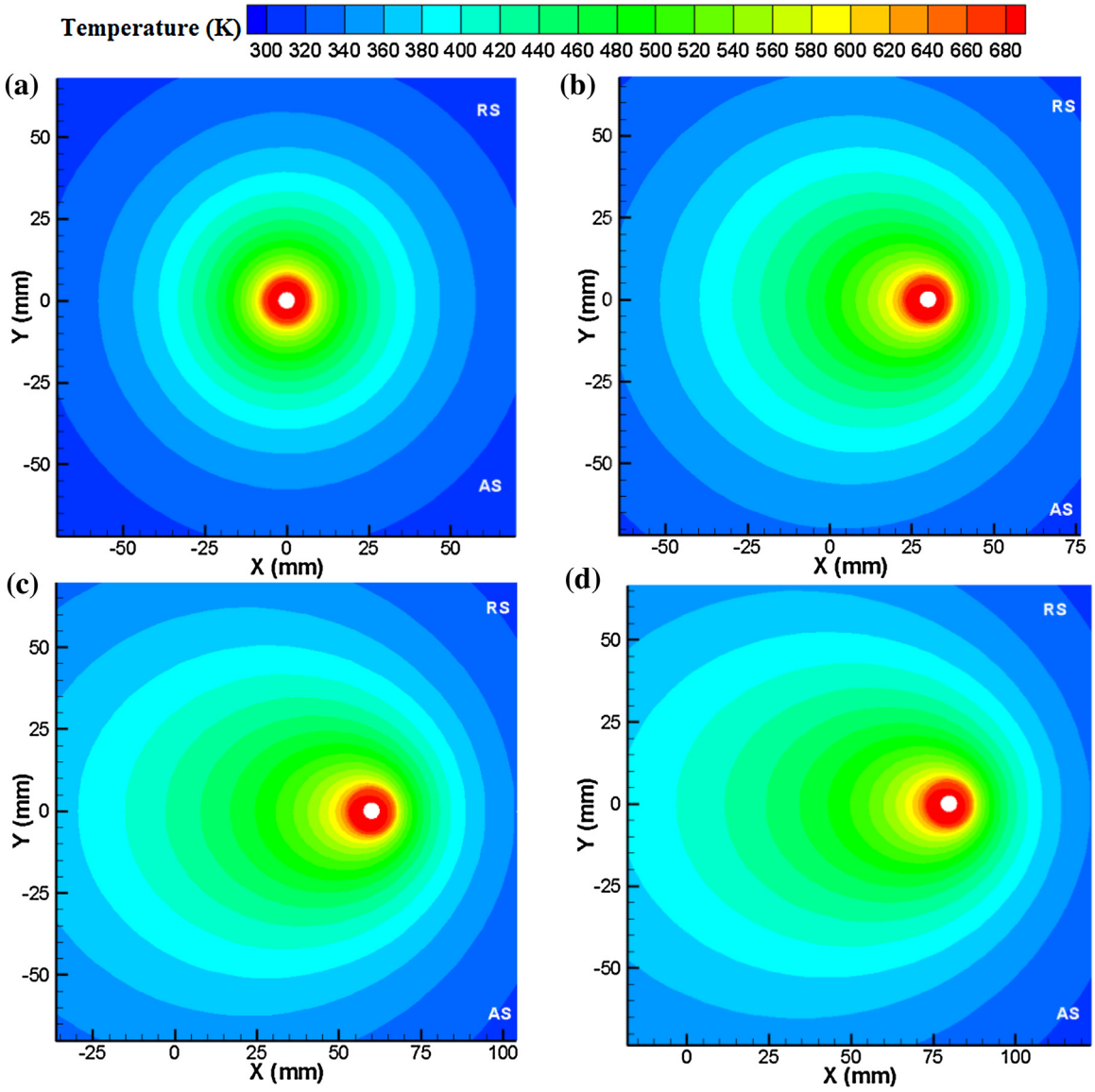


Fig. 11. The predicted temperature distribution at the top surface of the workpiece during the welding stage (Case 1). (a) 45.0 s, (b) 60.0 s, (c) 75.0 s, (d) 84.9 s.

bottom surface of the workpiece. However, at the late plunge stage (Fig. 9c and d), the hottest region is located at the pin bottom-workpiece contact interface. Another feature of the isothermals at the late plunge stage is that there is little temperature difference at the top and bottom surfaces of the workpiece. Fig. 9d also shows that at the end of the plunge stage, the temperature near the tool at the bottom of the workpiece is somewhat higher than that at the top surface because more heat is generated at the pin tip. In addition, the temperature profiles near the tool are almost identical on the AS and RS during the plunge stage, as shown in Fig. 9.

Fig. 10 illustrates the predicted temperature profiles at the transverse cross-section during the dwell stage and welding stage. After the shoulder contacts with the top surface of the workpiece, although the temperature near tool goes up sharply and the total heat generation is the maximum, the process temperature still doesn't reach its peak value. The peak value of temperature is actually reached during the welding stage. This is because the heat generation is instantaneous while heat transfer is time consuming. During the dwell stage, the temperature distribution is almost the same at the AS and the RS, as shown in Fig. 10a–d. However, the temperatures at the AS are slightly higher than that at the RS during the welding stage, as shown in Fig. 10e and f. Asymmetric temperature distribution exists near the pin due to the combined effect of tool rotation and translation during the welding stage. More heat is generated at the AS during the welding stage because the relative velocity and shear strain rate at AS is higher than that at RS. In addition, the material transported from behind the tool to the AS is relatively hotter than that transported from the front of the tool to the RS. It can be found that the calculated temperature profiles at 50.1 s (Fig. 10e) is similar to that at 60.0 s (Fig. 10f), which implies that a quasi-steady state heat transfer could be reached near the tool during the welding stage.

Fig. 11 shows the calculated temperature distribution on the top surface of the workpiece during the welding stage. At 45.0 s, the isothermals are axisymmetric about the tool axis before the tool starts to move, as shown in Fig. 11a. At the welding stage, the isothermals are elongated along the welding direction because of the tool translation and the density of isothermal contours in front of the tool is higher than that behind the tool. As the tool moves from its original position (X = 0 mm) to the position of X = 79.8 mm,

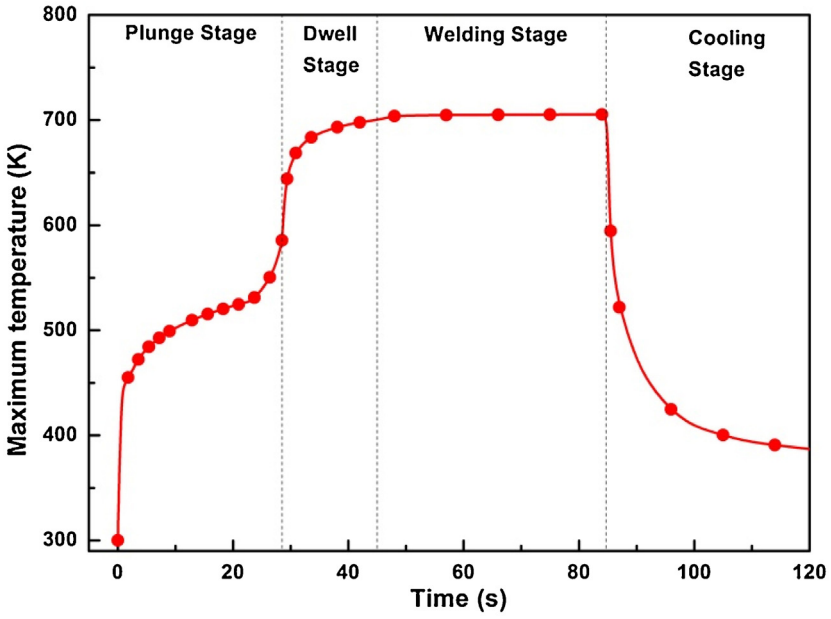


Fig. 12. The calculated peak temperature as a function of time during the FSW process (Case 1).

the contours are compressed in front of the tool and expanded behind the tool, as shown in Fig. 11b–d. Even though the isothermals near the tool at the transverse cross-section do not change too much after 50 s (as shown in Fig. 10e and f), the temperature distribution at the top surface of the workpiece changes with time and reaches to nearly quasi-steady state at 75 s, as shown in Fig. 11c and d. The relatively long time taken to establish the quasi-steady state condition demonstrates the limitations of the previous steady state models in analyzing the heat generation and material flow in FSW process [16–18]. In addition, the previous steady state models do not consider the heat generation and material flow during the plunge and dwell stages.

Fig. 12 shows the variation in calculated peak temperature with respect to time during FSW process. The peak temperature rapidly increases when the pin bottom just contacts the workpiece surface. The peak temperature rises slowly during most part of the plunge stage before increasing rapidly during the late plunge stage when the contact area between the pin and workpiece becomes sufficiently large. Further, when the shoulder contacts with the workpiece, the large amount of heat generated at the shoulder causes the peak temperature to sharply increase. In the dwell stage, the peak temperature increases miserly due to a decrease in total heat generation with increasing interfacial temperature. The peak temperature slightly increases during the early welding stage and subsequently becomes constant during the quasi-steady state of the welding stage. As the tool pulls out of the workpiece, the peak temperature decreases rapidly since there is no heat generation during the cooling stage. At the initial cooling stage, the cooling rate is relatively higher. After the peak temperature decreases to about 400 K, the cooling rate is lower.

4.3. Material flow field

Fig. 13 shows the calculated velocity of material flow near the tool at different moments in the FSW process. During the plunge stage, the plastic material rotates around the pin, as shown in Fig. 13a–c. Just before the contact between the shoulder and workpiece, the peak velocity of material flow is about 143 mm/s. After the shoulder contacts with the workpiece it increases rapidly to its peak value of 365 mm/s near the edge of the shoulder on the top surface of the workpiece (Fig. 13d). During the plunge stage, a relatively narrow region of the plastic material near the pin side is softened by the heat so that less material flows under the action of pin, as shown in Fig. 13a–c. After the shoulder contacts the workpiece, sufficient heat generation by the shoulder leads to softening of the material near the tool. As a result, the flow region near the tool expands, as shown in Fig. 13e. It should be noted that the flow distributions shown in Fig. 13e and f are identical. From these two figures, it is apparent that there is no significant change in the material flow behavior shortly after the shoulder contacts with the top surface of the workpiece.

The calculated strain rate at the transverse cross-section in FSW process is show in Fig. 14. At the initial plunge stage, the peak strain rate is located at the edge of the pin bottom (Fig. 14a and b). As the pin penetrate into the workpiece, the strain rate near the tool decreases (Fig. 14c) due to the increase in temperature near the tool. Just after the shoulder contacts the workpiece, the strain rate underneath the shoulder sharply increases to its peak value (Fig. 14d). From the peak, the strain rate at the shoulder-workpiece contact interface gradually decreases due to higher heat generation in this interface, which causes a decrease in the viscosity near the tool. During the dwell stage, the strain rate region in the tool vicinity increases and rapidly reaches the quasi-steady state (Fig. 14e and f). It could be found that the peak strain rate during the FSW process is located at the shoulder edge and the pin tip where the velocity gradient at these two locations is relatively large.

Fig. 15 demonstrates the calculated viscosity field near the tool at the transverse cross-section in FSW. The evolution of viscosity field near the tool illustrates similar trend to both the strain rate (Fig. 14) and the viscous dissipation heat generation (Fig. 8). In Fig. 15, the softened region has a viscosity lower than 1×10^7 kg m^{-1} s^{-1}. Since the heat generated at the tool-workpiece contact interfaces and thus the temperature near the tool at the initial plunge stage are low, the material softening takes place over a narrow region (Fig. 15a). As the pin penetrates into the workpiece, the softened region expands slightly (Fig. 15b and c). After the shoulder contacts with the top surface of the workpiece, the softened region expands sharply. Shortly after that the softened

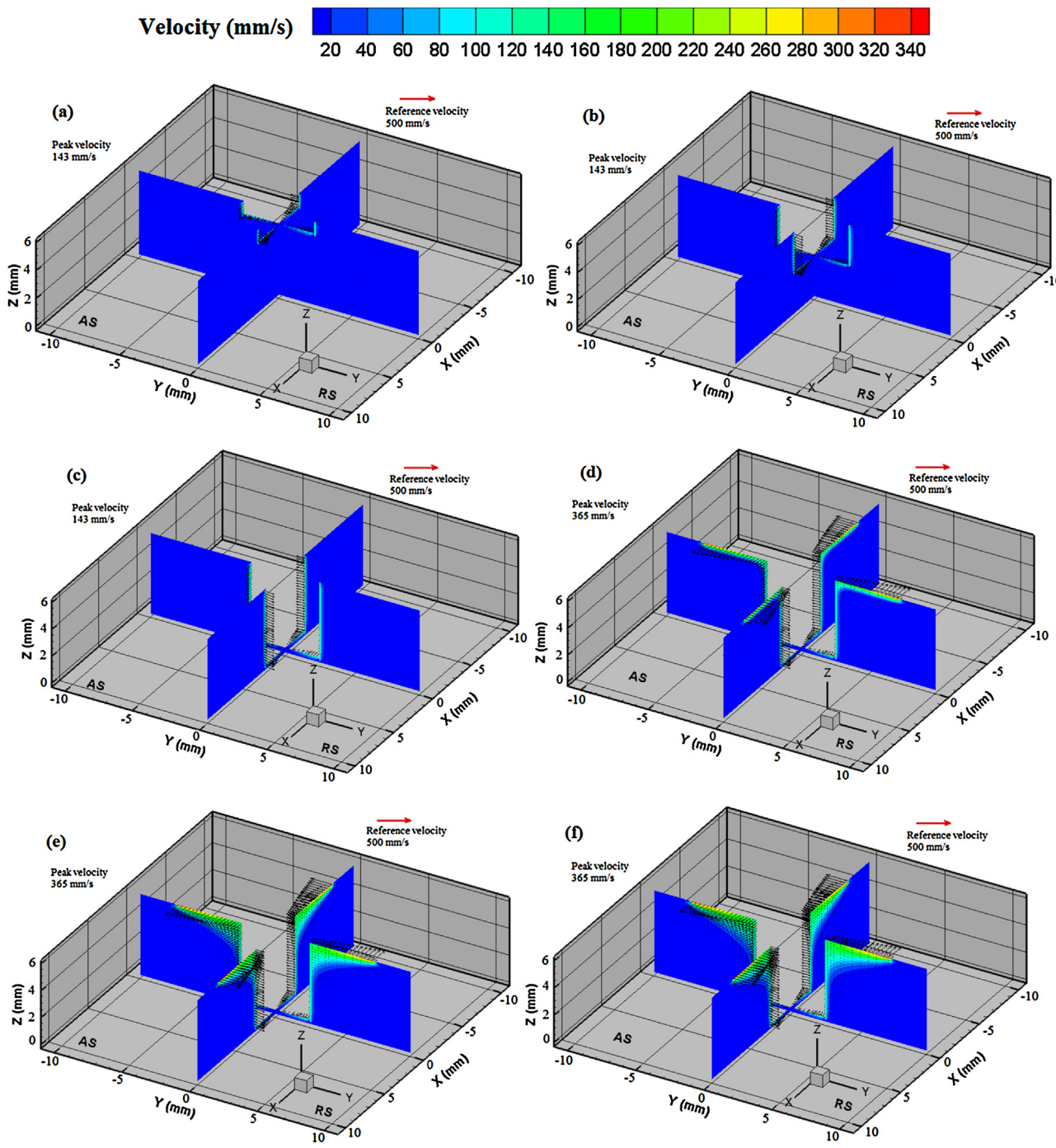


Fig. 13. The predicted material flow velocity near the tool in FSW process (Case 1). (a) 4.5 s, (b) 15.0 s, (c) 28.2 s, (d) 28.51 s, (e) 28.8 s, (f) 45.0 s.

region would remain constant at the dwell and welding stage, as shown in Fig. 15e and f.

Fig. 16 shows the material flow streamlines near the tool in the welding stage (t = 75.0 s) at horizontal plane (Z = 4 mm, i.e., 2 mm below the top surface of the workpiece). The plastically deformed material at the AS flows in counter-clockwise direction and passes the tool at the RS under the influence of the tool. Fig. 16 reveals that the material flow is largely influenced by the tool rotation speed and welding speed. When the welding speed is 120 mm/min (Case 1), the material at about 5.6 mm away from the joint line on the AS, i.e., at Y = −5.6 mm in front of the tool, flows in counter-clockwise direction and passes the tool at the RS (Fig. 16a). However, when the welding speed is 40 mm/min, a similar material flow is observed at Y = −6.5 mm (Case 3) as shown in Fig. 16b. From Fig. 16a and b, it is clear that the softened region near the tool is enlarged and more plastic material passes the tool at the RS with a decrease in the welding speed. Similarly, a comparison between Fig. 16c and d indicates that more plastic material near the tool at the AS flows and passes the tool at the RS with increasing rotation speed.

4.4. Experimental validation

The tool torque during the FSW process is coupled to heat generation and material flow because it depends on the process parameters, material properties and contact condition at the tool-workpiece contact interfaces [16–18]. The calculated and

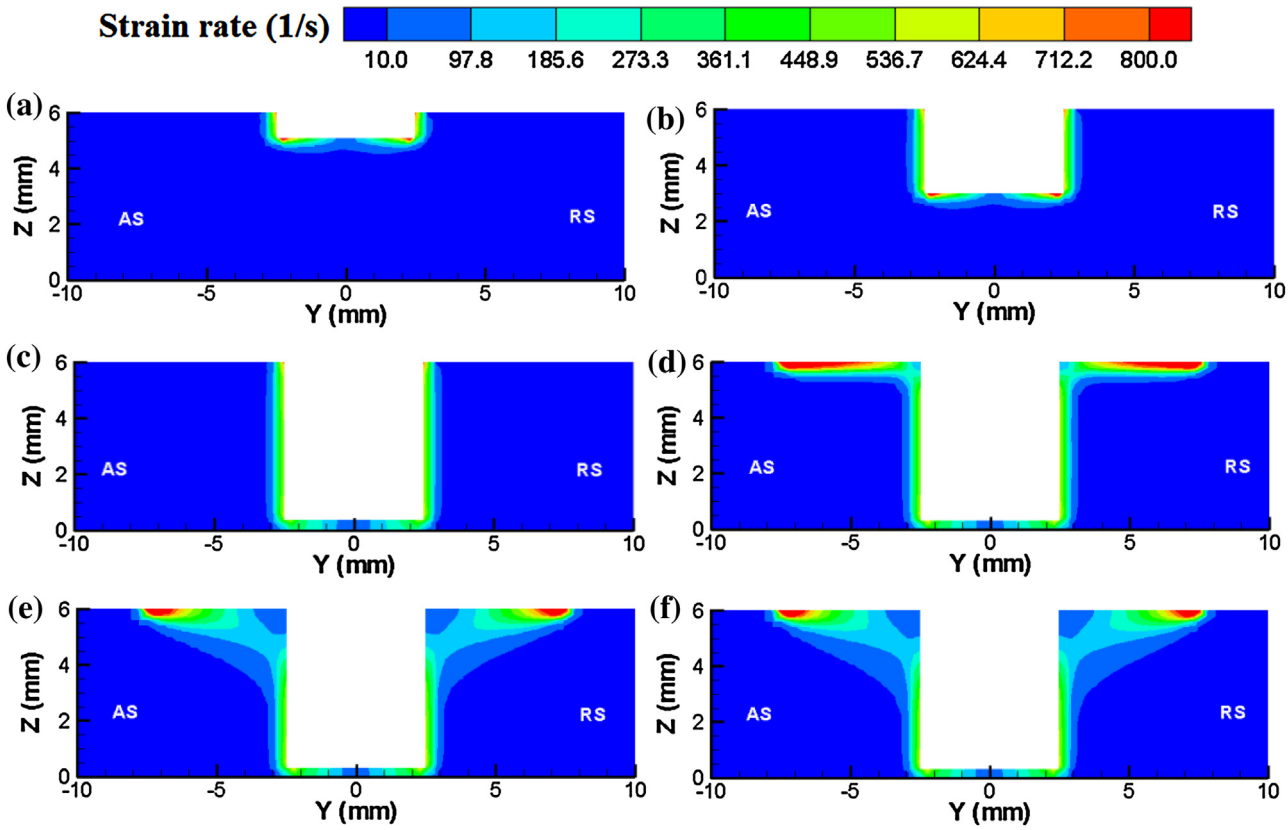


Fig. 14. The calculated strain rate at transverse cross-section in FSW process (Case 1). (a) 4.5 s, (b) 15.0 s, (c) 28.2 s, (d) 28.51 s, (e) 28.8 s, (f) 45.0 s.

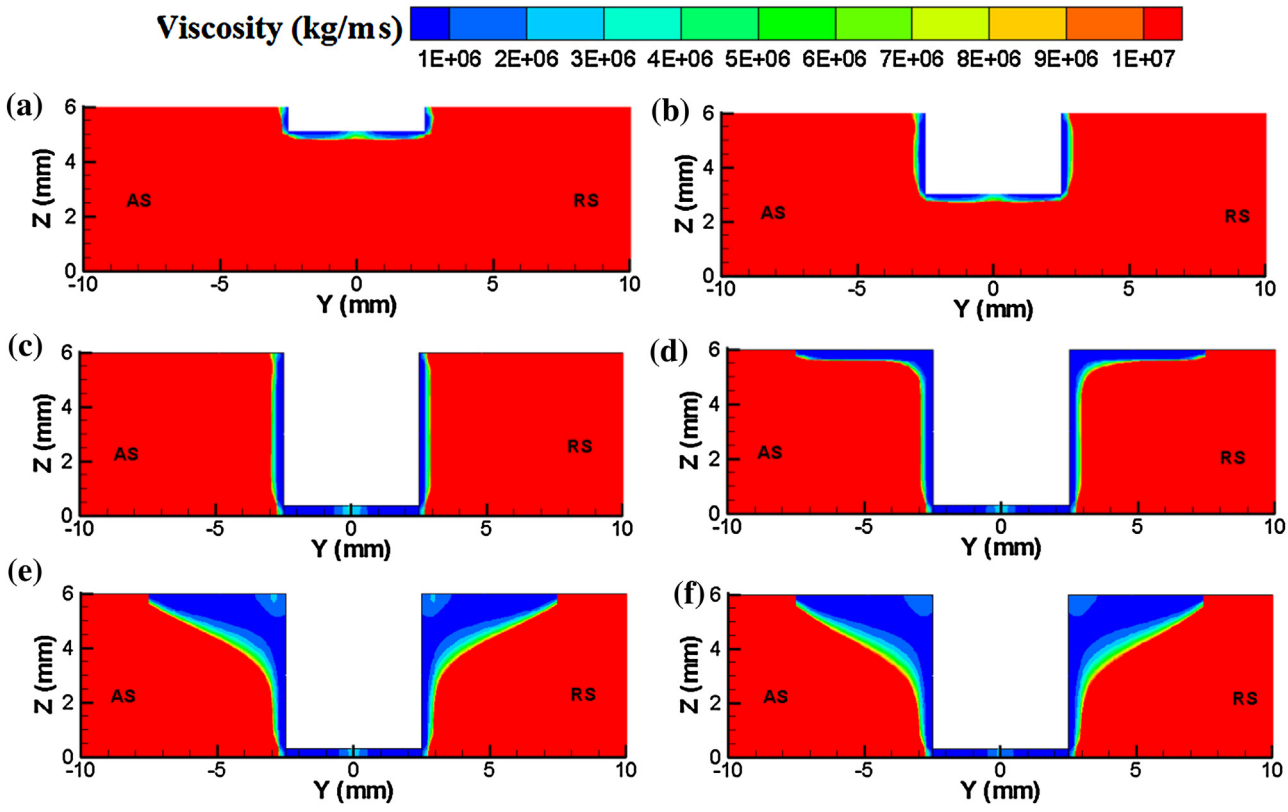


Fig. 15. The calculated viscosity field at transverse cross-section in FSW process (Case 1). (a) 4.5 s, (b) 15.0 s, (c) 28.2 s, (d) 28.51 s, (e) 28.8 s, (f) 45.0 s.

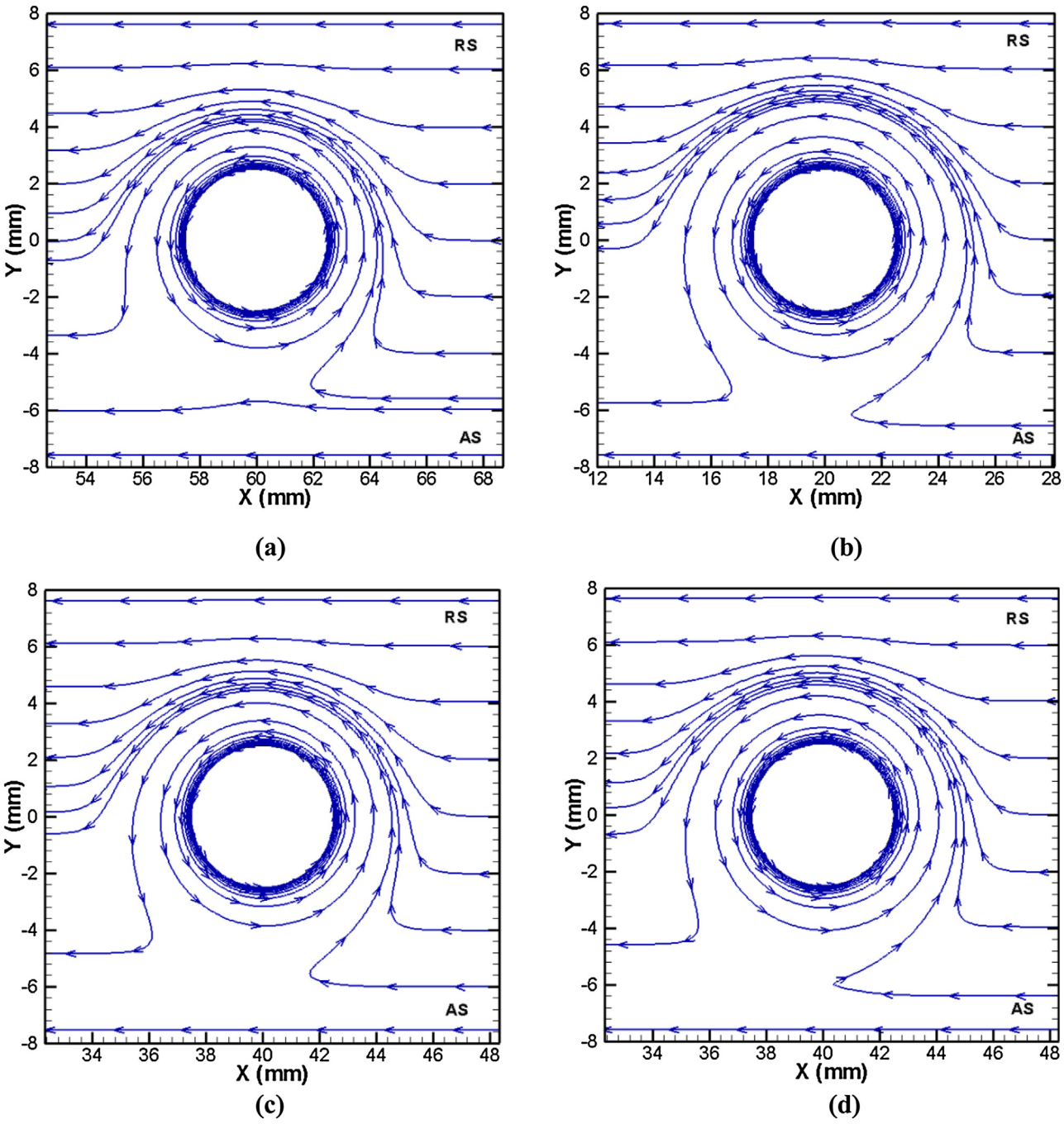


Fig. 16. The predicted streamlines near the tool during the welding stage (t = 75.0 s, Z = 4 mm). (a) Case 1, (b) Case 3, (c) Case 2, (d) Case 5.

experimentally measured tool torque and peak temperature can confirm the validity and reliability of the new transient model. Fig. 17 shows the comparison of the calculated tool torque with the experimentally measured results reported in literature [33]. In the transient model, the plunge and dwell stage was the same to the experimental condition, where the calculation of welding stage was shortened to reduce the calculation time of the model. It can be seen that both the calculated and measured tool torque are in good agreement with each other. Table 5 lists the comparison of the calculated and experimentally measured values of average tool torque during the quasi-steady state welding stage. The predicted tool torque agrees well with the experimentally measured values. Similarly, the comparison of the calculated peak

Table 5
Comparison of the measured and predicted tool torque at the quasi-steady state welding stage.

Case no.	Measured (Nm)	Calculated (Nm)	|Relative error| %
1	14.5	14.7	1.38
2	13.1	14.1	7.63
3	12.3	13.5	9.76
4	11.6	12.5	7.76
5	10.8	11.8	9.26
6	10.2	11.4	11.76

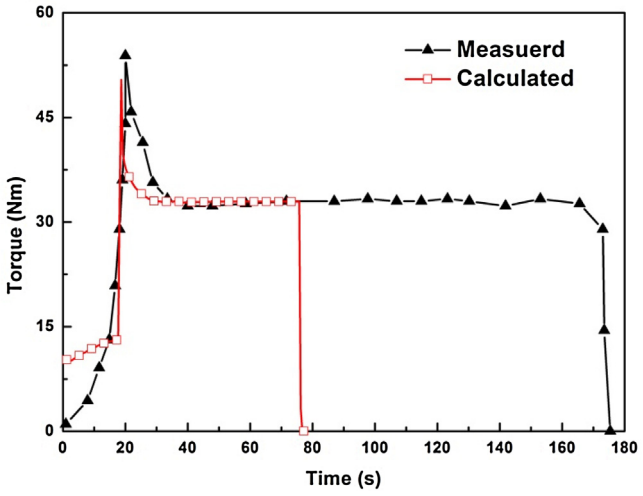


Fig. 17. Comparison of the calculated with the measured tool torque [33].

Table 6
Comparison of the measured and calculated peak temperature at some locations (Case 2).

Location coordinate (mm)		Measured	Calculated	|Relative error|
y-coordinate	z-coordinate	(K)	(K)	%
−5	2	651.70	648.73	0.05
−10	3	631.39	587.71	6.92
−15	3	506.69	534.81	5.55
−25	3	446.07	470.10	5.39

temperature at some locations with the experimentally measured values is presented in Table 6. It can be seen that the predicted peak temperatures at typical locations agree well with the measured ones. The above comparisons confirm the validity and reliability of the new model.

5. Summary and conclusions

A transient model is developed to analyze the heat generation, heat transfer and material flow for different stages of friction stir welding (FSW) process. It considers the interfacial heat generation due to both friction and plastic deformation at tool-workpiece contact interfaces and volumetric heat generation due to viscous dissipation near the tool. The model is confirmed to be reliable and valid from the good agreement between the predicted and measured values of tool torque and peak temperature. Important results obtained using this model regarding the heat generation, temperature distribution and the corresponding material flow behaviors are summarized as follows:

(1) Total heat generation increases monotonically during the plunge stage and sharply reaches to maximum at the end of this stage. It slowly decreases during the dwell stage and is almost constant during the welding stage. A change in the rotation speed is reflected by a similar change in heat generation during the plunge, dwell and welding stages whereas the change in welding speed only makes a variation of heat generation during the welding stage.
(2) Axisymmetric isothermal is clearly seen at the plunge and dwell stages, while the temperature at the advancing side is higher than that at the retreating side during the welding stage. The temperature distribution obtained from the transient model shows that achieving the quasi-steady state in the real FSW process is time consuming.
(3) The material flow behaviors mainly involves the counter-clockwise flow of the plastically deformed material in front of the tool that passes the tool at the retreating side and gets released behind the tool during the welding stage. The material flow region is found to be enlarged by decreasing the welding speed and/or by increasing the tool rotation speed.
(4) Variations in strain rate and viscosity during the different stages of the FSW process are analyzed. The peak strain rate during the plunge stage is located at the pin tip whereas it is located at the shoulder edges when the shoulder contacts with the workpiece during the dwell and welding stages.

Acknowledgment

This work is supported by the National Natural Science Foundation of China (Grant No. 51475272).

References

[1] Threadgill PL, Leonard AJ, Shercliff HR, Withers PJ. Friction stir welding of aluminium alloys. Int Mater Rev 2009;54(2):49–93.
[2] Mishra RS, Ma ZY. Friction stir welding and processing. Mater Sci Eng R Rep 2005;50(1–2):1–78.
[3] Nandan R, Debroy T, Bhadeshia HKDH. Recent advances in friction-stir welding-process, weldment structure and properties. Prog Mater Sci 2008;53:980–1023.
[4] He X, Gu F, Ball A. A review of numerical analysis of friction stir welding. Prog Mater Sci 2014;65:1–66.
[5] Wu CS, Zhang WB, Shi L, Chen MA. Visualization and simulation of the plastic material flow in friction stir welding of aluminium alloy 2024 plates. Trans Nonferrous Metals Soc China 2012;22:1445–51.
[6] Ulysse P. Three-dimensional modeling of the friction stir-welding process. Int J Machine Tools Manuf 2002;42:1549–57.
[7] Zhang Z, Chen JT, Zhang ZW, Zhang HW. Coupled thermo-mechanical model based comparison of friction stir welding processes of AA2024-T3 in different thicknesses. J Mater Sci 2011;46(17):5815–21.
[8] Soundararajan V, Zekovic S, Kovacevic R. Thermo-mechanical model with adaptive boundary conditions for friction stir welding of Al 6061. Int J Machine Tools Manuf 2005;45:1577–87.
[9] Assidi M, Fourment L, Guerdoux S, Nelson T. Friction model for friction stir welding process simulation: calibrations from welding experiments. Int J Machine Tools Manuf 2010;50:143–55.
[10] Cui S, Chen ZW, Robson JD. A model relating tool torque and its associated power and specific energy to rotation and forward speeds during friction stir welding/processing. Int J Machine Tools Manuf 2010;50:1023–30.
[11] Rai R, De A, Bhadeshia HKDH, DebRoy T. Review: friction stir welding tools. Sci Technol Weld Join 2011;16(4):325–42.
[12] Kuykendall K, Nelson T, Sorensen C. On the selection of constitutive laws used in modeling friction stir welding. Int J Machine Tools Manuf 2013;74:74–85.
[13] Zhang H, Huang JH, Lin SB, Wu L, Zhang JG. Temperature simulation of the preheating period in friction stir welding based on the finite element method. Proc Instit Mech Eng Part B J Eng Manuf 2006;220(7):1097–106.
[14] Chen CM, Kovacevic R. Finite element modeling of friction stir welding—thermal and thermomechanical analysis. Int J Machine Tools Manuf 2003;43(13):1319–26.
[15] Schmidt HB, Hattel JH. Thermal modelling of friction stir welding. Scr Mater 2008;58(5):332–7.
[16] Nandan R, Roy GG, DebRoy T. Three-dimensional heat and material flow during friction stir welding of mild steel. Acta Mater 2007;55(3):883–95.
[17] Cho HH, Hong ST, Roh JH, Choi HS, Kang SH, Steel RJ, et al. Three-dimensional numerical and experimental investigation on friction stir welding processes of ferritic stainless steel. Acta Mater 2013;61(7):2649–61.
[18] Su H, Wu CS, Pittner A, Rethmeier M. Thermal energy generation and distribution in friction stir welding of aluminum alloys. Energy 2014;77:720–31.
[19] Arora A, De A, DebRoy T. Toward optimum friction stir welding tool shoulder diameter. Scr Mater 2011;64(1):9–12.
[20] Fratini L, Buffa G. CDRX modelling in friction stir welding of aluminium alloys. Int J Machine Tools Manuf 2005;45:1188–94.
[21] Hamilton C, Dymek S, Sommers A. A thermal model of friction stir welding in aluminum alloys. Int J Machine Tools Manuf 2008;48(10):1120–30.
[22] Yu Z, Zhang W, Choo H, Feng ZL. Transient heat and material flow modeling of friction stir processing of magnesium alloy using threaded tool. Metal Mater Trans A 2012;43(2):724–37.
[23] Song M, Kovacevic R. Thermal modeling of friction stir welding in a moving coordinate system and its validation. Int J Machine Tools Manuf 2003;43(6):605–15.
[24] Zhang XX, Xiao BL, Ma ZY. A transient thermal model for friction stir weld. Part I: the model. Metal Mater Trans A 2011;42(10):3218–28.
[25] Zhang XX, Xiao BL, Ma ZY. A transient thermal model for friction stir weld, part II: effects of weld conditions. Metal Mater Trans A 2011;42(10):3229–39.

[26] Chen G, Shi Q, Li Y, Sun Y, Dai Q, Jia J, Zhu Y, Wu J. Computational fluid dynamics studies on heat generation during friction stir welding of aluminum alloy. Comput Mater Sci 2013;79:540–6.
[27] Chen G, Feng Z, Zhu Y, Shi Q. An alternative frictional boundary condition for computational fluid dynamics simulation of friction stir welding. J Mater Eng Perform 2016;25(9):4016–23.
[28] Shi L, Wu CS, Liu HJ. Analysis of heat transfer and material flow in reverse dual-rotation friction stir welding. Weld World 2015;59(5):629–38.
[29] Arora A, Nandan R, Reynolds AP, DebRoy T. Torque, power requirement and stir zone geometry in friction stir welding through modeling and experiments. Scr Mater 2009;60(1):13–6.
[30] Shi L, Wu CS, Gao S, Padhy GK. Modified constitutive equation for use in modeling the ultrasonic vibration enhanced friction stir welding process. Scr Mater 2016;119:21–6.
[31] Mandal S, Rice J, Elmustafa AA. Experimental and numerical investigation of the plunge stage in friction stir welding. J Mater Process Technol 2008;203(1):411–9.
[32] Gemme F, Verreman Y, Dubourg L, Jahazi M. Numerical analysis of the dwell phase in friction stir welding and comparison with experimental data. Mater Sci Eng A 2010;527(16):4152–60.
[33] Trimble D, Monaghan J, O'Donnell GE. Force generation during friction stir welding of AA2024-T3. CIRP Ann Manuf Technol 2012;61(1):9–12.
[34] Shi L, Wu CS, Liu HJ. The effect of the welding parameters and tool size on the thermal process and tool torque in reverse dual-rotation friction stir welding. Int J Machine Tools Manuf 2015;91:1–11.
[35] Colegrove PA, Shercliff HR, Zettler R. Model for predicting heat generation and temperature in friction stir welding from the material properties. Sci Technol Weld Join 2007;12(4):284–97.
[36] Nandan R, Roy GG, Debroy T. Numerical simulation of three-dimensional heat transfer and plastic flow during friction stir welding. Metal Mater Trans A 2006;37(4):1247–59.
[37] Sellars CM, Tegart W. Hot workability. Int Metal Rev 1972;17(1):1–24.
[38] Sheppard T, Jackson A. Constitutive equations for use in prediction of flow stress during extrusion of aluminum alloys. Mater Sci Technol 1997;13:203–9.
[39] Shi L, Wu CS, Padhy GK, Gao S. Numerical simulation of ultrasonic field and its acoustoplastic influence on friction stir welding. Mater Design 2016;104:102–15.
[40] Mehta M, Chatterjee K, De A. Monitoring torque and traverse force in friction stir welding from input electrical signatures of driving motors. Sci Technol Weld Join 2013;18(3):191–7.
[41] Shi L, Wu CS, Liu HJ. Numerical analysis of heat generation and temperature field in reverse dual-rotation friction stir welding. Int J Adv Manuf Technol 2014;74(1-4):319–34.
[42] Versteeg HK, Malalasekera W. An introduction to computational fluid dynamics: the finite volume method. 2nd ed. Glasgow, UK: Pearson Education; 2007.
[43] ANSYS FLUENT Release Version 14.5. ANSYS Inc., Documentation, 2012.
[44] Su H, Wu CS, Pittner A, Rethmeier M. Simultaneous measurement of tool torque, traverse force and axial force in friction stir welding. J Manuf Processes 2013;15:495–500.
[45] Li T, Shi QY, Li HK. Residual stresses simulation for friction stir welded joint. Sci Technol Weld Join 2007;12(8):664–70.
[46] Bastier A, Maitournam MH, Dang K, Roger F. Steady state thermomechanical modelling of friction stir welding. Sci Technol Weld Join 2006;11(3):278–88.